Astronomy & Astrophysics manuscript no. aa56303-25
April 14, 2026
©ESO 2026

arXiv:2604.11677v1 [astro-ph.GA] 13 Apr 2026

Do little red dots really form a distinct class of astronomical objects?

Jean-Baptiste Billand[1] ⋆, David Elbaz[1], Maximilien Franco[1], Fabrizio Gentile[1,2], Emanuele Daddi[1], Mauro Giavalisco[3], Dale D. Kocevski[4], Joseph S. W. Lewis[1], Benjamin Magnelli[1], Valentina Sangalli[1], and Maxime Tarrasse[5,6]

[1] Université Paris-Saclay, Université Paris Cité, CEA, CNRS, AIM, 91191, Gif-sur-Yvette, France
[2] INAF – Osservatorio di Astrofisica e Scienza dello Spazio, via Gobetti 93/3 - 40129, Bologna - Italy
[3] University of Massachusetts Amherst, 710 North Pleasant Street, Amherst, MA 01003-9305, USA
[4] Department of Physics and Astronomy, Colby College, Waterville, ME 04901, USA
[5] School of Astronomy and Space Science, Nanjing University, Nanjing 210093, China
[6] Key Laboratory of Modern Astronomy and Astrophysics, Nanjing University, Ministry of Education, Nanjing 210093, China

ABSTRACT

Observations with the James Webb Space Telescope (JWST) have identified a previously unidentified class of enigmatic sources, known as “Little Red Dots” (LRDs), that are also relatively abundant in space. These sources have been interpreted as a distinct class of active galactic nuclei (AGN) and host galaxies whose structural properties, e.g. the mass of the SMBH and the emissivity from the associated AGN, as well as the stellar mass of the host galaxy or the possibility of so-called "quasi stars" or Black Hole star (BH*), suggesting the existence of a previously unidentified class of extragalactic objects. Two questions, however, have yet to be addressed before invoking a new paradigm: is there a clear discontinuity between the properties of the LRDs and field galaxies at the same cosmic epochs, and do LRDs form a single homogeneous population? In this work, we address these two issues by introducing a continuous metric to evaluate the "LRDness" of galaxies. We measure their compactness ($\delta_{\rm compact}$), the sharpness of the V-shaped ($\delta_{\rm v\text{-}shape}$) spectral energy distribution (SED), and the strength of the broad Balmer line emission. We apply this approach, which avoids imposing a binary “on/off” view of the population, to a sample of $\approx$ 48,000 ($\approx$ 5,000) galaxies with photometric (spectroscopic) information, selected over an area of $\approx$750 arcmin^2. We find that the prominence of the V-shaped SED exhibits a strong correlation with morphology without any clear transition at the commonly used LRD selection threshold: the fraction of compact galaxies rises with the V-shape intensity. Similarly, the strength of the Hα broad line component increases with the V-shape sharpness and with compactness. We also note that the deficit of [N II] itself is not an exclusive feature of LRDs but a global property of compact, metal-poor galaxies. Finally, only a minority of LRDs - the 3 % most extreme ones - present a prominent Balmer break of potentially non-stellar origin (greater than 3). We also find that LRDs and non-LRDs follow similar trends in the evolution of the Balmer decrement with the V-shape sharpness suggesting that this evolution originates from the same physical cause, the favored one being dust attenuation. The dust masses ($\approx 4-7\times10^4 M_\odot$) and luminosities involved are low enough to account for their non-detection by ALMA. In conclusion, our results suggest that, apart from a minority of a few percent, LRDs at large do not represent a separate class of objects, but rather the extreme tail of a continuous distribution of galaxies and broad Hα emitters. Most LRDs appear to be consistent with a classical broad line region and a dust component.

Key words. Galaxies: formation – Galaxies: evolution

1. Introduction

The James Webb Space Telescope has opened one of the most intriguing chapters in early-Universe studies: the discovery of red, compact sources exhibiting broad Balmer lines (e.g., Labbé et al. 2023; Kocevski et al. 2023; Furtak et al. 2023; Kokorev et al. 2024), hereafter referred to as Little Red Dots (Matthee et al. 2024). These objects were initially interpreted as either dusty AGNs (e.g., Kocevski et al. 2025; Matthee et al. 2024; Greene et al. 2024) or dusty, compact massive galaxies (Labbé et al. 2023; Baggen et al. 2026; Pérez-González et al. 2024). However, subsequent observations have placed stringent constraints on their dust content. In particular, the flattening of the mid-infrared (MIR) SED appears incompatible with the presence of a hot dust torus (Williams et al. 2024; Pérez-González et al. 2024). When combined with non-detections in the far-infrared (FIR), these limit the potential dust reservoir in LRDs (Akins et al. 2025; Casey et al. 2024; Xiao et al. 2025; Setton et al. 2025). This evidence challenges both the highly obscured AGN and the dusty star-forming scenarios, where dust was previously considered the primary driver of the observed red colors.

The discovery of unique sources, MOM-z-BH*1 and "the Cliff" (Naidu et al. 2025; de Graaff et al. 2025c), also challenged all previously proposed scenarios. These objects display Balmer breaks that are incompatible with a purely stellar component, and standard AGN templates hardly reproduce this feature (Ma et al. 2025; de Graaff et al. 2025c). Similar sources were subsequently identified (Taylor et al. 2025b; Barro et al. 2026), and to explain such prominent Balmer breaks, an extremely dense gas reservoir along the line of sight has been invoked (Ji et al. 2025; Inayoshi & Maiolino 2025). Based on these observables, models featuring a Black Hole (BH) embedded in extremely dense gas, the so-called *BH** model, have recently been proposed (e.g.,

⋆ jean-baptiste.billand@cea.fr

Naidu et al. 2025; de Graaff et al. 2025c; Rusakov et al. 2026; Begelman & Dexter 2026; Santarelli et al. 2026). This scenario is rooted in the theoretical framework of "quasi-stars" originally developed by Begelman et al. (2008). In this framework, the dense layer surrounding the BH thermalizes and emits as a modified blackbody in the rest-frame optical and near-infrared.

Furthermore, within the BH* model, broad lines arise not from a virialized Broad Line Region (BLR) as in the standard AGN paradigm (e.g., Greene & Ho 2005; Reines & Volonteri 2015), but through physical processes such as electron or resonance scattering (e.g., Naidu et al. 2025; Torralba et al. 2026; Rusakov et al. 2026; Chang et al. 2026). This interpretation would imply BH masses nearly two orders of magnitude lower than those typically inferred. However, several LRDs appear to be inconsistent with this picture. For instance, a dynamical BH mass was measured for one source (Juodžbalis et al. 2025), showing agreement with the mass estimated from the Hα line. Additionally, a multi-line analysis of the "Rosetta Stone" LRD disfavored resonance and electron scattering as the primary mechanism for line broadening (Juodžbalis et al. 2026; Brazzini et al. 2025). While the BH* model predicts the X-ray weakness observed in most LRDs (Begelman & Dexter 2026; Pacucci et al. 2026; Kido et al. 2025), several LRDs have now been detected in X-rays (Kocevski et al. 2025; Fu et al. 2025; Hviding et al. 2026). These observations support the idea that not all LRDs can be classified purely as BH* objects as proposed, indicating that a more complex physical picture is required.

Moreover, the definition of LRDs varies depending on the applied selection criteria, leading to classification ambiguities for sources near the boundaries. Consequently, an object's classification as an LRD may depend solely on specific sample limits. For instance, various color-color selections have been developed (e.g., Kocevski et al. 2025; Kokorev et al. 2024; Akins et al. 2025; Barro et al. 2024), each introducing slightly different thresholds that result in significantly different sample compositions. Models built on solely conservative selections likely miss less extreme objects, creating a biased view of the population. This implies that broad-line Balmer emitters located near these selection boundaries can be interpreted either as BH* objects or as typical AGNs, which are two orders of magnitude more massive, depending on arbitrary selection cuts.

This raises a fundamental question: purely on observables, do LRDs represent a distinct class of astronomical objects? To address this, we propose a new metric to characterize the features of LRDs, specifically their compactness and V-shaped SED. Unlike traditional color-color cuts, this approach avoids arbitrary binary thresholds by treating these characteristics as continuous parameters, $\delta_{\rm compact}$ and $\delta_{\rm v\text{-}shape}$.

We investigate in this work, using this continuous approach, whether LRDs exhibit discontinuities in their observed properties with galaxy fields, which would make appear a natural selection for them and signifying a separate population, or if they demonstrate continuous behavior, suggesting instead that they form a continuum with the broader galaxy population. To address this, we combine photometric, and spectroscopic data over the four widest fields covered by the JWST: PRIMER-UDS, PRIMER-COSMOS, JADES (GS+GN), and CEERS, as described in Section 2. In Section 3, we introduce a continuous approach to quantify the main features of LRDs. Section 5 focuses on the behavior of the Hα emission line, and we discuss the physical interpretation of our findings within the LRD framework in Section 7. Magnitude used are in the AB system (Oke 1974) and the cosmological parameters from Planck Collaboration et al. (2020).

2. Data

2.1. Photometric data

In this work, we utilize publicly available photometric catalogs from several JWST surveys. We specifically select fields providing coverage in at least the following six NIRCam wide-band filters: F115W, F150W, F200W, F277W, F356W, and F444W. These data are supplemented by the Hubble Space Telescope (HST) observations in the F606W and F814W bands from ACS/WFC (Davis et al. 2007; Ford et al. 1998). This comprehensive multi-band coverage enables an accurate determination of both rest-frame optical and UV slopes between $2 < z < 10$, as detailed in Section 3. The surveys used in this study are described below:

- JWST Advanced Deep Survey (JADES; Eisenstein et al. 2026; Hainline et al. 2024; Rieke et al. 2023): We use the official DR2 and DR3 photometric catalogs for the GOODS-N and GOODS-S fields, covering approximately 175 arcmin^2 and F444W$_{5\sigma\ \text{point-source}} = 29.62$. Photometric redshifts provided in these catalogs were computed using `EAZY` (Brammer et al. 2008), with $\sigma_{\rm NMAD}$[1] ≈ 0.037.
- Cosmic Evolution Release Science (CEERS; Finkelstein et al. 2017, 2023): Located in the EGS field and covering 97 arcmin^2 and F444W$_{5\sigma\ \text{point-source}} = 28.97$. We adopt the official catalog from Cox et al. (2025), which includes both photometry and photometric redshifts determined with `LePHARE` (Arnouts et al. 1999; Ilbert et al. 2006), with $\sigma_{\rm NMAD} \approx 0.035 - 0.073$.
- Public Release IMaging for Extragalactic Research (PRIMER; Dunlop et al. 2021): This survey covers $\approx$ 500 arcmin^2 across the COSMOS and UDS fields (PRIMER-COSMOS and PRIMER-UDS) with F444W$_{5\sigma\ \text{point-source}} = 28.2 - 28.5$. We use the photometric catalogs provided by Sun et al. (2026a) along the photometric redshift computed with EAZY, $\sigma_{\rm NMAD} \approx 0.027$.

The catalogs already include spectroscopic redshifts when available, which we supplement with data from the DAWN JWST Archive (DJA, v4.4). More details are provided in Section 2.2. To ensure robust photometric detections and reliable redshift estimates, we exclude sources with a signal-to-noise ratio below 10 in F444W ($S/N < 10$). Furthermore, for sources lacking spectroscopic redshifts, we remove those with poorly constrained photometric redshifts with $\chi^2_{\rm phot} > 15$.

2.2. Spectroscopic data

Throughout this work, we utilize the spectroscopic data available on DJA, the NIRSpec MSA spectra table (version 4.4). The spectra were reduced using the `msaexp v0.9.8` pipeline (Brammer 2023), following the methodology described in Heintz et al. (2025) and de Graaff et al. (2025a), see de Graaff et al. (2025b) for further details. For PRISM data, we exclusively use spectra with a `grade = 3`, ensuring high-quality data and forming a sample of approximately 17,000 spectra from numerous surveys[2] (e.g., CEERS: Finkelstein et al. 2025, JADES: Eisenstein et al. 2026; D'Eugenio et al. 2025; Curtis-Lake et al. 2025; Scholtz et al. 2025, NEXUS: Shen et al. 2024, UNCOVER:

[1] The parameter $\sigma_{\rm NMAD}$ represents the scatter in the photometric versus spectroscopic redshift relation, defined as $1.48 \times \text{median}\left(\frac{|\Delta z - \text{median}(\Delta z)|}{1+z_{\rm spec}}\right)$, where $\Delta z = z_{\rm phot} - z_{\rm spec}$.

[2] See dawn-cph/dja/spectroscopy/nirspec for a complete list.

Bezanson et al. 2024; Price et al. 2025, GTO-Wide: Maseda et al. 2024, CAPERS: GO-6368; PI: Dickinson, RUBIES: de Graaff et al. 2025a).

Next, we merge the PRISM data with our photometric catalog (by cross-matching at 0.1 arcsec), including the spectroscopic redshifts where possible. For the analysis in Section 5, we also use the GRISM and grating data provided by the DJA.

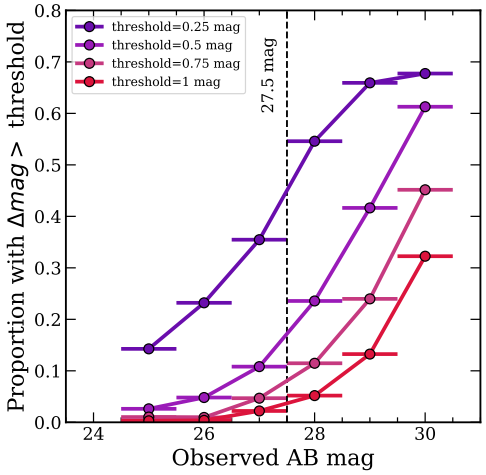

Fig. 1. Illustration of the Hα boosting effect: the proportion of galaxies for which the Hα line in PRISM spectra coincides with either the F277W, F356W, or F444W filters, requiring a correction in AB magnitude above specific thresholds (from 0.25 AB mag in purple to 1 AB mag in red), is plotted as a function of the observed AB magnitude.The vertical dashed line denotes a magnitude of 27.5 AB. Below this limit, fewer than 20% of the galaxies require a correction exceeding 0.5 mag.

3. Evaluating the LRDness in galaxies : δ_{compact} & $\delta_{\text{v-shape}}$

To determine whether LRDs represent a distinct population with unique observed properties compared to other galaxies, or whether they lie along a continuum, exhibiting progressively more extreme properties, we adopt an approach that is as agnostic as possible regarding their selection. Specifically, we eliminate any a priori assumptions about their properties and selection criteria. To achieve this, we construct a continuous scale applicable to all galaxies, based on two key parameters: δ_{compact} and $\delta_{\text{v-shape}}$. The first parameter, δ_{compact}, quantifies the galaxy's compactness. The second, $\delta_{\text{v-shape}}$, measures the prominence of the V-shaped SED, characterized by the combination of a red rest-frame optical continuum and a blue rest-frame UV continuum.

These two parameters capture the two primary characteristics of LRDs: a V-shaped SED and a compact morphology, but on a continuous scale. The spectroscopic analysis of the Hα line, the third key property of LRDs, is done a posteriori in Section 5, given the relatively limited availability of spectroscopic data.

3.1. On the Hα contribution to the observed broad band flux

One of the potential biases in photometric studies, and consequently in the measurement of the $\delta_{\text{v-shape}}$ parameter, arises from the boosting effect of emission lines within broad filters. This is particularly relevant for LRDs when computing the optical slope, β_{opt}, as discussed in Kocevski et al. (2025). The Hα line flux can boost the last filter used to compute the optical slope, and therefore we can overestimate the redness of LRDs in photometric studies. To quantify this bias, we utilize the public NIRSpec MSA v4.4 table available on the DJA (see Section 2.2). We focus on PRISM spectra where the Hα line falls within the red broad bands of the JWST, specifically in the F277W, F356W, or F444W filters. We then measure the Hα flux for approximately 5,000 sources in the corresponding filter by employing :

$$F_{\text{H}\alpha,\text{filter}} = \frac{\int f_{\lambda,\text{H}\alpha}\, T(\lambda)\, \mathrm{d}\lambda}{\int T(\lambda)\, \mathrm{d}\lambda}, \tag{1}$$

where $T(\lambda)$ represents the transmission curve of the filter, and $F_{\text{H}\alpha,\text{filter}}$ denotes the flux of the Hα line measured by the corresponding filter. To isolate the Hα line ($f_{\lambda,\text{H}\alpha}$) from the PRISM data, we first subtract the continuum using a power-law fit. We then extract the spectral region within a 0.2 μm window centered on the Hα emission. This isolated line profile is resampled onto a broader wavelength grid that matches the transmission profile of the corresponding filter, after which we apply Equation (2).

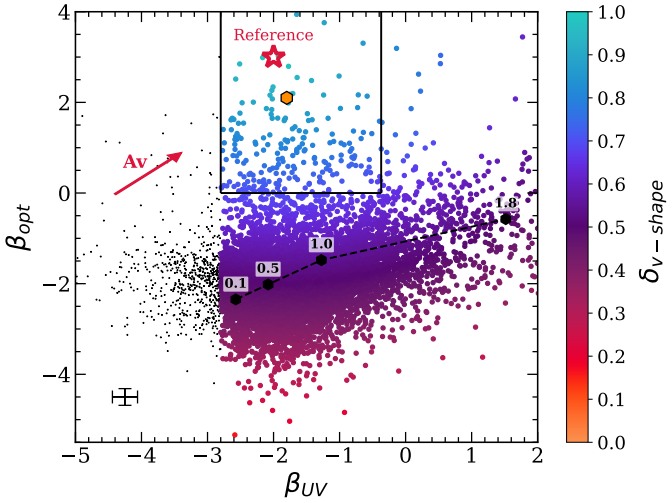

Fig. 2. Distribution of sources in the β_{UV}–β_{opt} plane for the PRIMER-UDS field, illustrating the $\delta_{\text{v-shape}}$ parameter. Higher values of $\delta_{\text{v-shape}}$ (approaching 1) indicate a more prominent V-shaped SED. The selection criteria from Kocevski et al. (2025) are overlaid as solid black lines for comparison. The red star represents the reference point ($\beta_{\text{UV,ref}} = -2, \beta_{\text{opt,ref}} = 3$) used to derive $\delta_{\text{v-shape}}$. A typical error bar for the ($\beta_{\text{UV}}, \beta_{\text{opt}}$) measurements is shown as a cross in the bottom-left corner. The red vector illustrates the effect of increasing dust attenuation on the stellar population, assuming a Calzetti et al. (2000a) law. The dotted line represents the evolutionary track of a dust-free galaxy, assuming a delayed star formation history with a fixed $\tau = 200$ Myr and a stellar age evolving from 0.1 to 1.8 Gyr. For reference, we include CEERS 746 (orange hexagon), a broad-line AGN studied by Kocevski et al. (2023), whose optical colors can be explained by either a dusty starburst galaxy or a obscured quasar.

Figure 1 illustrates the fraction of sources requiring a correction in AB magnitude above fixed values (0.25, 0.5, 0.75, and 1 mag) as a function of the observed AB magnitude (in either F277W, F356W, or F444W). The contribution of Hα to the observed flux is inversely related to the source brightness: at 28 AB mag, approximately 55% of galaxies observed in filters covering Hα require a correction exceeding 0.25 AB mag. This fraction decreases gradually for brighter sources. As expected, fewer galaxies require larger corrections, only 25% at 28 AB mag need

a correction above 0.5 mag, and less than 10% require a correction above 1 mag.

We conclude that applying a threshold of 27.5 AB mag in broad-band filters covering Hα (here after denoted $m_{\mathrm{H}\alpha}$) ensures minimal contamination from line emission: fewer than 20% of galaxies will require a correction above 0.5 mag, and fewer than 10% will need a correction above 0.75 mag. We caution that this analysis does not account for the magnitude limits of individual fields, and variations in this threshold are expected for shallower or deeper surveys. Moreover, extended galaxies might need a more important correction due to slit-loss. Nevertheless, this provides a quantitative estimate of the Hα boosting effect. Consequently, LRDs fainter than 27.5 AB mag should not be selected using photometric methods, as their red colors may be significantly contaminated by this effect. All along this work we therefore apply the following threshold: we limit the magnitude of the filter containing Hα to be brighter than 27.5 AB mag, $m_{\mathrm{H}\alpha}$<27.5 AB mag. Applied to a subsample of 41 LRDs (from Kocevski et al. 2025 sample), the correction applied to the optical slope β_{opt} is on average 0.18.

3.2. Intensity of the V-shape : $\delta_{\text{v-shape}}$

LRDs are typically selected using thresholds in either color-color or color-magnitudes diagrams (Labbe et al. 2025; Greene et al. 2024; Pérez-González et al. 2024; Kokorev et al. 2024; Barro et al. 2024; Akins et al. 2025; Rinaldi et al. 2025a) or based on their rest-frame optical–UV slope, β_{UV} and β_{opt}, which presents a blue UV continuum and a red optical continuum (Kocevski et al. 2025; Leung et al. 2025; Hviding et al. 2025; de Graaff et al. 2025b). However, as these thresholds are arbitrary, the delimitation and definition of LRDs remain non-unified and strongly depend on the authors and available data. Consequently, objects near the selection boundary are sensitive to the method applied. For instance, the color-color selection of Barro et al. (2024) tends to include more objects than that of Kocevski et al. (2025).

This raises a fundamental question: Can these *less extreme* candidates, which are missed by conservative selection criteria, be interpreted as members of the LRD population? Do they exhibit the same properties, or do they belong to another class? To address this fundamental question, we first introduce the following parameter: $\delta_{\text{v-shape}}$.

To achieve this, we compute the rest-frame UV slope, β_{UV}, and the rest-frame optical slope, β_{opt}, as described in Kocevski et al. (2025), using the photometric data presented in Section 2.1. These slopes are defined by the relation $f_\lambda \propto \lambda^\beta$, where the slopes on the blue side correspond to β_{UV} and slopes on the red side to β_{opt}, measured on either side of the Balmer break at 3645 Å. At different redshift intervals, the set of bands switch accordingly to always probe the two regions of interest. Between $2 < z < 8$, both the UV slope and optical slopes are computed with 3 filters each, whereas at higher redshift $z > 8$, the optical slope is computed only with two bands (see Kocevski et al. (2025) for more details). We then define the parameter $\delta_{\text{v-shape}}$ as follows:

$$\delta_{\text{v-shape}} = 1 - \frac{\sqrt{(\beta_{\mathrm{UV}} - \beta_{\mathrm{UV,ref}})^2 + (\beta_{\mathrm{opt}} - \beta_{\mathrm{opt,ref}})^2}}{10}, \quad (2)$$

with $(\beta_{\mathrm{UV,ref}}, \beta_{\mathrm{opt,ref}})$ representing a reference point in the $\beta_{\mathrm{UV}}, \beta_{\mathrm{opt}}$ plane. The parameter $\delta_{\text{v-shape}}$ is therefore defined as the Euclidean distance from an arbitrary point, normalized to a maximum distance (here, 10). This reference point is chosen to correspond to an extreme V-shape: $(\beta_{\mathrm{UV,ref}} = -2, \beta_{\mathrm{opt,ref}} = 3)$. An illustration of $\delta_{\text{v-shape}}$ is provided in Figure 2 for the PRIMER-UDS field. To avoid contamination by brown dwarfs, we exclude sources with $\beta_{\mathrm{UV}} < -2.8$ (Greene et al. 2024; Kocevski et al. 2025). In Figure 2, we also display a fiducial dust-free galaxy track. This track was generated using `CIGALE` (Boquien et al. 2019) to model the SED, assuming a delayed star formation history with a fixed e-folding time of $\tau = 200$ Myr and a stellar population age evolving from 0.1 to 1.8 Gyr. The impact of dust reddening is represented by a red vector, calculated assuming a Calzetti et al. (2000b) attenuation law. For comparison, we include CEERS 746, an LRD previously studied by Kocevski et al. (2023). The optical SED of this source is degenerate, as it can be well-described by either a reddened Type 1 QSO or a dusty starburst galaxy.

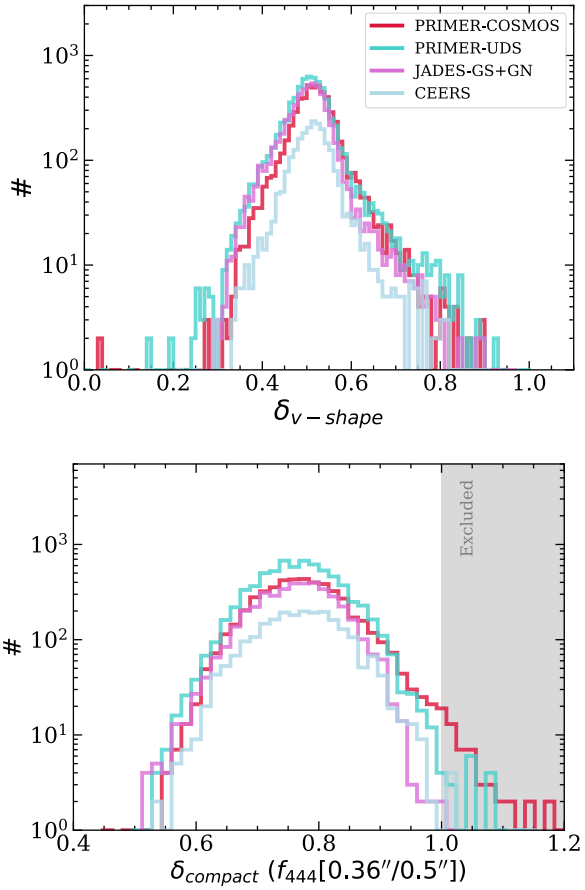

Fig. 3. Top: Distribution of the parameter $\delta_{\text{v-shape}}$ for every fields used in this work. As $\delta_{\text{v-shape}}$ approaches 1, more extreme is the V-shaped SED. Bottom: Distribution of δ_{compact} in every fields use in this work, as δ_{compact} increases, galaxies are more compact. In shaded gray we show the excluded region to avoid artifacts.

This parameter offers the advantage of being a continuous scale that evaluates the intensity of the V-shape, without excluding less extreme objects. Based on this scale, a galaxy with a $\delta_{\text{v-shape}}$ value close to one exhibits an extreme V-shaped SED, whereas the majority of galaxies present a less intense V-shaped SED, with $\delta_{\text{v-shape}} \approx 0.5$, as shown by the top panel in Figure 3. The distribution remains consistent across all fields, indicating

that the measurement of this parameter is independent of the field used, thus enabling reliable comparisons between fields.

3.3. Compactness : $\delta_{compact}$

To quantify the compactness of the galaxies in our sample, we utilize the public data from the DJA. By cross-matching our photometric catalog across all fields (at 0.1″), we incorporate the aperture photometry provided by the DJA in the F444W filter. Following a similar methodology as in Greene et al. (2024); Kokorev et al. (2024); Akins et al. (2025); Barro et al. (2024), we employ an aperture flux ratio to define source compactness. Since this approach is model-independent, it avoids the convergence issues that can appear in 2D Sersic fits for sources near the resolution limit, particularly in the case of LRDs. Given that the specific apertures provided by the DJA differ from those used in the literature, we define our compactness parameter, $\delta_{\rm compact}$, as:

$$\delta_{\rm compact} = \frac{f_{444}(d = 0.36'')}{f_{444}(d = 0.5'')} \,. \tag{3}$$

Similar to the C_{444} parameter used by Akins et al. (2025), this ratio can be sensitive to artifacts or hot pixels at extreme values. To mitigate these effects, we clip the $\delta_{\rm compact}$ distribution at the same sigma-level from the median to match the threshold applied by Akins et al. (2025). In our sample, this corresponds to a cut at $\delta_{\rm compact} = 1$; we therefore exclude any sources with values exceeding this limit. Furthermore, to minimize the redshift dependence of $\delta_{\rm compact}$ (which is based solely on the F444W band), we restrict our analysis to $3 < z < 9$. This ensures that we are probing the rest-frame compactness within the $\approx$ 0.5–1.1 μm range. This parameter utilizes fluxes within aperture diameters of 0.36″ and 0.5″. While this differs from the apertures commonly used in the literature (typically 0.2″ and 0.4″ or 0.5″), we compare C_{444} and $\delta_{\rm compact}$ in Appendix A and show that both are strongly correlated. Therefore, $\delta_{\rm compact}$ is also an efficient proxy to probe compact objects. By cross-matching our catalog with the morphological measurements provided by the DJA (using a 0.1″ radius; Genin et al. 2025), we derive a median half-light radius of $R_e = 0.076^{+0.10}_{-0.05}$ arcsec for sources with $\delta_{\rm compact} > 0.8$. This median value lies below the Half-Width at Half-Maximum (HWHM) of the F444W Point Spread Function (PSF; $\approx$ 0.08 arcsec), confirming that the majority of the sources above this compactness value are point-source dominated.

3.4. Summary of the sample selection

Here we summarize the steps and selection criteria applied to form our final sample:

- We exclude sources with poorly constrained photometric redshifts, defined as those with $\chi^2_{\rm phot} > 15$ when spectroscopic redshifts are not available.
- We require the S/N in F444W to be above 10.
- We require the filter covering the Hα line to be brighter than 27.5 AB mag (i.e., $m_{\rm H\alpha} < 27.5$).
- Brown dwarfs are removed by applying an UV slope cut of $\beta_{\rm UV} > -2.9$.
- Sources with $\delta_{\rm compact} > 1$ are excluded.
- The sample is restricted to $3 < z < 9$.

Our final sample is composed of 47,928 sources, among which 7,072 have spectroscopic redshifts. A subsample of 5,185 sources possesses PRISM data covering Hα, and 2,960 have data with a higher-resolution grating (Medium or High).

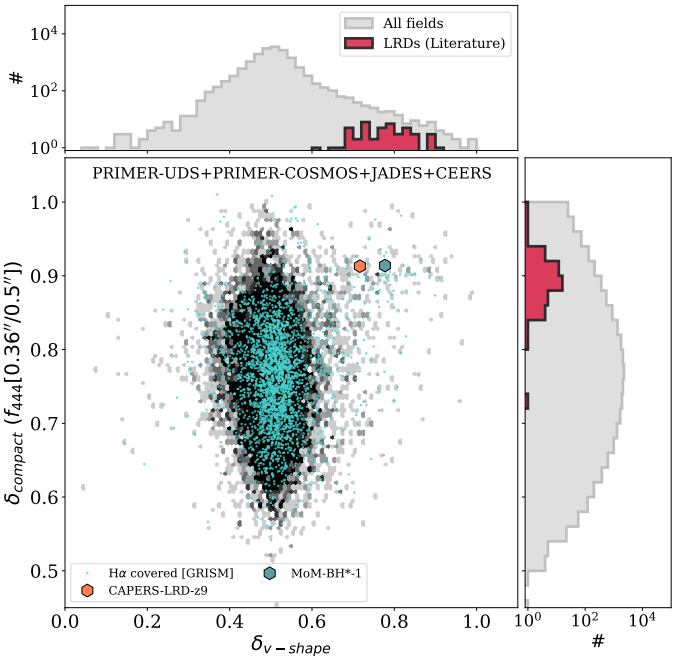

Fig. 4. $\delta_{\rm compact}$ as a function of $\delta_{\rm v\text{-}shape}$, for all the galaxies in every fields studied: PRIMER-UDS, PRIMER-COSMOS, JADES-GS, JADES-GN and CEERS. Cyan points correspond to galaxy for which Hα covering from at least GRISM medium resolution is available. Cyan and orange hexagon represent Mom-BH*-1 and CAPERS-LRD-z9 from Naidu et al. (2025) and Taylor et al. (2025b), respectively. In the corner plots, the red histograms represent the merged LRD sample from Kocevski et al. (2025) and Akins et al. (2025), while the grey histograms show the distribution of the entire galaxy population.

4. Correlation between $\delta_{\rm v\text{-}shape}$ and $\delta_{\rm compact}$

The first aspect we investigate is the potential correlation between the V-shaped SED in galaxies and their compactness, combining data from all fields. In Figure 4, we first present $\delta_{\rm compact}$ as a function of $\delta_{\rm v\text{-}shape}$, along with the available spectroscopic data (medium and high resolution that covered Hα used in Section 5).

By cross-matching the LRDs sample of Kocevski et al. (2025) and Akins et al. (2025), we determine typical values for LRDs to be $\delta_{\rm v\text{-}shape} > 0.6$ with $\delta_{\rm compact} > 0.8$. As expected, typical LRDs are located in the upper-right region of the diagram. For reference, we also highlight two extreme LRDs[3] on Figure 4, *CAPERS-LRD-z9* and *MoM-BH*-1* (Taylor et al. 2025b; Naidu et al. 2025).

Based on Figure 4, we observe that a significant proportion of galaxies with strong $\delta_{\rm v\text{-}shape}$ values also tend to be compact. This is supported by the left panel of Figure 5, which illustrates the fraction of compact galaxies as a function of their V-shape intensity, $\delta_{\rm v\text{-}shape}$. As the SED in galaxies becomes more V-shaped, their morphology tends to be more compact. This result aligns with findings by Hviding et al. (2025), who used a smaller sample from the RUBIES survey (de Graaff et al. 2025a), where a large portion ($\approx$ 75 – 80%) of galaxies with V-shaped SEDs were identified as point sources. However, this is the first time such a correlation is shown with high statistics: $\approx$ 1370 sources respecting $\delta_{\rm v\text{-}shape} > 0.5$ and $\delta_{\rm compact} > 0.8$, forming the red curve

[3] We note that *The Cliff* from de Graaff et al. (2025c) is blended with a foreground source in F444W, making the measurement of $\delta_{\rm compact}$ not relevant.

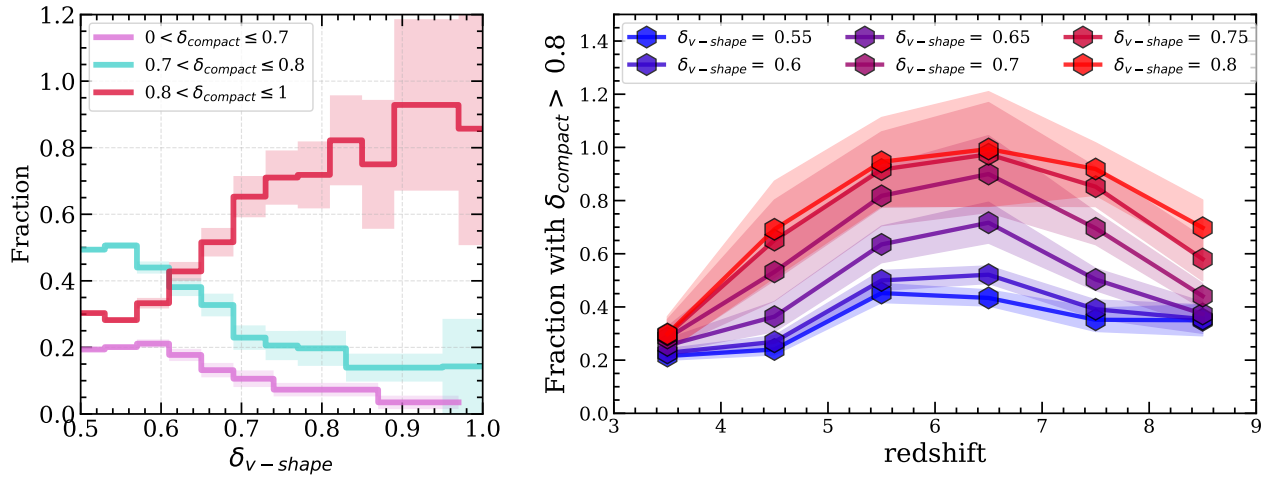

Fig. 5. Left: Fraction of galaxies (within a given $\delta_{\rm compact}$ interval) as a function of $\delta_{\rm v\text{-}shape}$, the intensity of the V-shape. The errors correspond to Poissonian errors. Right: Fraction of compact galaxies, with a given V-shape intensity from $\delta_{\rm v\text{-}shape} = 0.5$ to $\delta_{\rm v\text{-}shape} = 0.8$, as a function of redshift.

on Figure 5-left, indicating that compactness is an intrinsic property of galaxies with intense V-shaped SEDs.

Moreover, we do not observe sharp transitions, even around the LRD boundaries ($\delta_{\rm v\text{-}shape} \approx 0.6$). Instead, the fraction of compact galaxies increases with the intensity of the V-shape. This shows a continuous relationship between the continuum properties ($\delta_{\rm v\text{-}shape}$) and morphology ($\delta_{\rm compact}$) and a global transition towards higher LRD state. At $\delta_{\rm v\text{-}shape} = 0.6$, $\approx$ 30% of galaxies exhibit $\delta_{\rm compact} > 0.8$, whereas at $\delta_{\rm v\text{-}shape} = 0.75$, it increases to $\approx$ 70% of the galaxies. There is therefore a non-negligible number of galaxies that share the same continuum properties as LRDs but are extended, a population that dominates up to $\delta_{\rm v\text{-}shape} \approx 0.7$. Beyond this value, compact galaxies dominate, despite large uncertainties due to the lack of statistics.

We notice that the curve that represents the amount of compact galaxies ($\delta_{\rm compact} > 0.8$) as a function of the intensity of the V-shape (red curve on Figure 5-left) has a sigmoid shape. By fitting a sigmoid function per interval of redshifts from $z = 3$ to $z = 8$ (see Appendix B), we are also able to probe the amount of compact galaxies at a given V-shape intensity and a given redshift, which is displayed on Figure 5-right. We recover the typical redshift range for LRDs, between $4 < z < 8$ (e.g., Kocevski et al. 2025; Akins et al. 2025; Ma et al. 2026), with a peak around $z \approx 6$. Given the magnitude threshold applied ($m_{\rm H\alpha}$<27.5 AB mag; see Section 3.1), the decline at the high-redshift end is likely due to incompleteness, as also discussed in Kocevski et al. (2025) and Pacucci et al. (2023). Additionally, we observe a similar redshift-dependent behavior for all $\delta_{\rm v\text{-}shape} > 0.5$ values, with an increase in the contribution of compact galaxies as the intensity of the V-shape increases. The steepness of the decline between $4 < z < 5$ strongly evolves with $\delta_{\rm v\text{-}shape}$, with a steeper decline for intense V-shaped sources. This suggests a shorter life time of such extreme sources, potentially quickly evolving to more extended, less V-shaped objects (Billand et al. 2026).

In the following sections, we focus on the subsample for which spectroscopic data are available (see Section 3.4). Given that we have previously quantified the contribution of Hα emission to the broadband filters (see Section 3.1) and are working with relatively small statistics, we choose to correct our optical slope measurements (and consequently $\delta_{\rm v\text{-}shape}$) for this effect. Although this correction is minor, as discussed at the end of Section 3.1, we hereafter denote the corrected value as $\delta^c_{\rm v\text{-}shape}$. Typically, the correction applied to sources with $\delta_{\rm v\text{-}shape} > 0.6$ is approximately 0.01. The $\delta_{\rm v\text{-}shape}$ intervals used in the figures throughout this work are at least four times larger than this value, ensuring that the observed trends remain independent of this correction.

4.1. Evolution of the Balmer break strength

Several extreme LRDs exhibit, alongside other properties, a Balmer break strength incompatible with a stellar origin (Ji et al. 2025; Naidu et al. 2025; de Graaff et al. 2025c; Taylor et al. 2025b). In de Graaff et al. (2025b), it was suggested that the optical emission in LRDs originates from a modified black body, which would form extreme Balmer breaks with a temperature of $T_{\rm BB} \approx 5000$ K.

Therefore, we sought to investigate this alternative property, as the Balmer break strength could serve as a distinguishing feature for the LRD population. To compute the Balmer break strength, we adopt the same definition as described in de Graaff et al. (2025c), using the ratio of the mean flux density between [3620, 3720] Å and [4000, 4100] Å. We utilize the PRISM spectra available on the DJA, retaining only those that match our photometric catalog (see Section 2.2). After excluding measurements with low robustness (S/N < 2), we retain ≈5000 sources with robust Balmer break measurements. It is important to note that computing $\beta_{\rm opt}$ following the method of Kocevski et al. (2025) relies on broadband filters where the bluest data point remains redward of the Balmer break. Consequently, this photometric approach probes redder wavelengths that do not overlap with the spectral range used to calculate the Balmer break strength spectroscopically. In this work, these two quantities are therefore distinct and independent of the method used to compute the optical slope. This contrasts with Barro et al. (2026), where the optical slope is calculated across the Balmer break (from 0.3μm to 0.9μm rest-frame), inherently correlating the optical slope and Balmer break strength by construction.

In Figure 6, we present the Balmer break strength as a function of $\delta_{\rm compact}$ across different bins of V-shape intensity: $\delta^c_{\rm v\text{-}shape} < 0.55$, $0.55 < \delta^c_{\rm v\text{-}shape} < 0.65$, and $\delta^c_{\rm v\text{-}shape} > 0.65$. These three bins represent non-V-shaped, intermediate, and intense V-shaped sources, respectively. We then compute the median Balmer break for each $\delta_{\rm compact}$ bin, ensuring that each bin contains at least 15 sources. For the $0.55 < \delta^c_{\rm v\text{-}shape} < 0.65$ and

$\delta^c_{\text{v-shape}} < 0.55$ cases, we require 50 sources per bin to reduce the total number of bins and improve visual clarity. Surprisingly, as we go towards compact V-shape sources, we do not observe a clear trend for them to present a prominent Balmer break. Effectively, the most extreme bin ($\delta_{\text{compact}} > 0.9$ & $\delta^c_{\text{v-shape}} > 0.65$), presents a median value of $1.3^{+2.8}_{-0.98}$ similar to the median values of other bins. More generally, no distinct behavior is visible regardless of galaxy morphology or continuum shape. On a subsample of 37 LRDs from Kocevski et al. (2025), we infer a Balmer break strength of $1.4^{+2.2}_{-0.98}$, in agreement with our values in the LRD regime.

For all the Balmer break strengths computed ($\approx$ 5000), the most extremes ones are observed in *CAPERS-LRD-z9* and *MoM-BH*-1*. Given the absence of a correlation between compactness, V-shape intensity, and Balmer break strength, sources with prominent Balmer breaks appear as outliers, even within the usual LRD population. Effectively, sources with a Balmer break strength exceeding 3 account for only $\approx$ 3% of those exhibiting both a V-shape ($\delta^c_{\text{v-shape}} > 0.6$) and a compact morphology ($\delta_{\text{compact}} > 0.8$).

This demonstrates that the majority of LRDs do not exhibit a prominent Balmer break, as the median value remains between 1 and 1.5 for both extended and compact galaxies, regardless of the V-shape prominence. Coupled with the large scatter observed in compact, V-shaped galaxies, this implies that the population probed in the high LRD regime is not homogeneous.

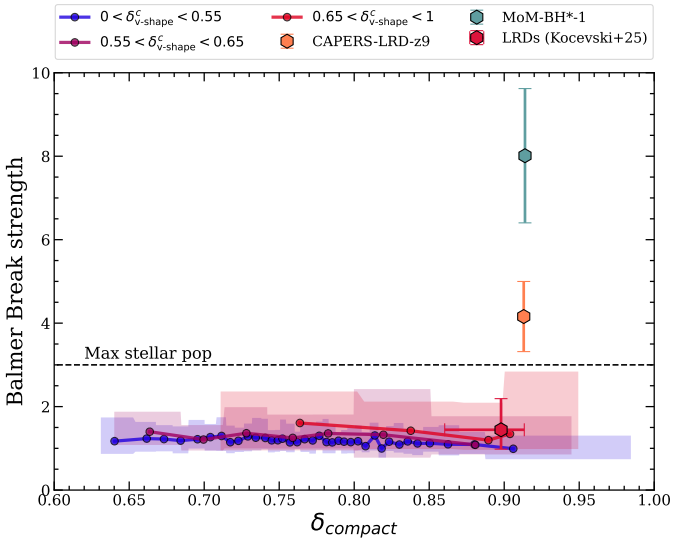

Fig. 6. Balmer break strength as a function of δ_{compact} for three bins of $\delta_{\text{v-shape}}$. Shaded regions correspond to the 1-sigma uncertainties for each bin: the vertical extent represents the 16th and 84th percentiles, while the horizontal width indicates the bin size. The dashed horizontal line denotes the maximum Balmer break strength of stellar origin observed to date (Naidu et al. 2025). The distribution of 37 LRDs from Kocevski et al. (2025) sample is shown as a red hexagon. Cyan and orange hexagon represent Mom-BH*-1 and CAPERS-LRD-z9 from Naidu et al. (2025) and Taylor et al. (2025b), respectively. Only robust measurements with $S/N > 2$ are included in this figure.

5. Behavior of the Hα+ [N II] complex as a function of $\delta_{\text{v-shape}}$, δ_{compact}

5.1. Method of the Hα line analysis

We have observed that morphology and continuum are strongly correlated (see Section 4) but LRDs exhibit a third key property: the presence of broad Hα and Hβ lines. Given that the Hα line is the brightest, we focus exclusively on its behavior.

To resolve and decompose the Hα complex, we restrict our analysis to the NIRSpec GRISM grating, which offers both medium ($R \approx 1000$) and high resolution ($R \approx 3000$).

To investigate the evolution of the Hα line shape, that is, the contribution of the broad component as a function of the continuum ($\delta^c_{\text{v-shape}}$) and compactness ($\delta_{\text{compact}}$), we first divide the galaxies into two groups: compact ($0.8 < \delta_{\text{compact}} < 1$) and extended ($0.6 < \delta_{\text{compact}} < 0.8$). Then, we stack the GRISM spectra per bin of $\delta^c_{\text{v-shape}}$. This approach allows us to first investigate any global behavior as galaxies approach the LRD state, while also increasing the S/N, particularly in the wings of the Hα lines, where the broad component might otherwise remain undetected or partially detected.

To achieve this, we select only the GRISM spectra with confirmed spectroscopic redshifts. Each spectrum is then shifted to the rest-frame. To prevent artificial broadening during stacking, arising from uncertainties in the spectroscopic redshift, we refine the redshift by aligning the peak emission of the Hα complex, these corrections remain within a few spectral bins (typically < 5). Then, each line is normalized to 1, and all spectra are resampled onto a uniform grid. After visual inspection, we excluded 9 sources from the compact group due to the Hα line being near detector edges. This exclusion ensures the highest data quality, especially given the limited statistics of the compact group. Since the majority of the spectra were observed with the G395M filter (see Table 1), we resampled all spectra onto a grid with a resolution of $0.0018/(1+z)\,\mu$m per bin, corresponding to the maximum dispersion of G395M. Finally, we compute the median to obtain the median stack in each bin of δ_{compact} and $\delta^c_{\text{v-shape}}$. To estimate the uncertainty corresponding to the median, we employ a Monte Carlo (MC) approach. Each individual spectrum is re-simulated 5000 times by incorporating Gaussian noise, where the noise amplitude is determined by the individual error associated with each spectrum. For each simulation, we compute the median spectrum from the noisy spectra. The standard deviation of the resulting distribution of these median spectra is then used as the uncertainty for the median spectrum. To maximize the signal-to-noise ratio (S/N), we defined our bins of $\delta_{\text{v-shape}}$ with a minimum of 16,000 seconds of effective exposure time. The detailed configuration of these bins is presented in Table 1. Our final spectroscopic sample include $\approx$340 spectra for compact galaxies, and $\approx$886 for extended galaxies, with a V-shape intensity between $\delta_{\text{v-shape}}$=0.6 and 1.

Once the median spectra and their associated uncertainties are constructed, we employ `BADASS v10.2.0` (Sexton et al. 2021) to decompose the Hα complex. Originally designed for analyzing spectra from the Sloan Digital Sky Survey (SDSS), this pipeline is highly adaptable and suitable for JWST spectra. It utilizes a Bayesian approach for all parameters, effectively mitigating issues related to local convergence. The decomposition of the Hα complex is performed as follows:

- Narrow Hα line: This component is fitted with a Gaussian profile, allowing three free parameters: Amplitude (`AMP`), Width (σ) and Velocity offset (`voff`).
- Broad Hα line: This component is also fitted with a Gaussian profile, but with only two free parameters: Amplitude (`AMP`), Width (σ). The velocity offset (`voff`) is constrained to be the same as that of the narrow Hα line.

– [N II] doublet ([NII]λ6585 and [NII]λ6549): Both lines are fitted with Gaussian profiles, but with only one free parameter: Amplitude (`AMP`) of the [NII]λ6585 line.
The width (σ) and the velocity offset (`voff`) of both lines are constrained to be the same as those of the narrow Hα line. Additionally, the flux of the [N II] λ6549 line is constrained by atomic physics: by fixing the line width, we constrain the amplitude such that $\texttt{AMP}_{\texttt{[NII]6549}} = \texttt{AMP}_{\texttt{[NII]6585}} \times 0.341$ (Osterbrock & Ferland 2006).

The model used to describe the Hα complex includes a total of six free parameters. Additionally, a power law component is incorporated to account for any potential continuum contribution, introducing two further parameters. To ensure physically meaningful results, priors are imposed on the model parameters: the widths of the narrow lines are restricted to the range $0 < \sigma_{\rm narrow} < 500$ km s^{-1}, while the width of the broad line is confined to $500 < \sigma_{\rm broad} < 1500$ km s^{-1}. Furthermore, the velocity offsets of all lines are constrained within the interval $-800 <$ `voff` < 800 km s^{-1}. To evaluate the presence of the broad component, we re-fit all the spectra without including a broad component and compute the Bayesian Information Criterion (BIC) parameter. We consider that a broad component is effectively present and necessary when ΔBIC = BIC$_{\rm narrow}$ − BIC$_{\rm narrow+broad}$ exceeds 5 (see Appendix C) and the S/N of the broad component is above 5, similar criterion has been employed in other broad line detection works (e.g., Juodžbalis et al. 2025; Taylor et al. 2025a; Brooks et al. 2025).

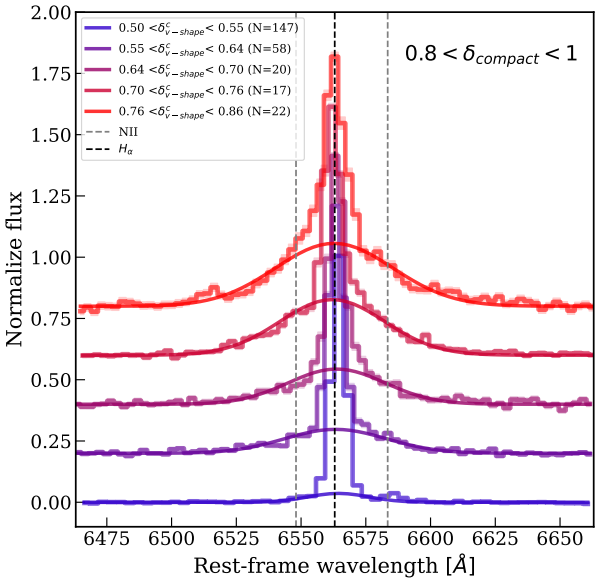

Fig. 7. Stacked spectra of the Hα complex along with the result of the broad Hα fit. Each spectrum is offset for clarity. The legend specify each bin of $\delta_{\rm v\text{-}shape}$ and the number of spectra used (always having an effective exposure time above 16,000s), details on the bins can be seen on Table 1.

5.2. Result of the Hα decomposition

In Figure 7, we show the stacked spectra for each bin of compact galaxies ($0.8 < \delta_{\rm compact} < 1$) with the results of the broad line fit. For each bin of $\delta^c_{\rm v\text{-}shape}$, the presence of the broad component is strongly favored, with a minimum S/N of 9 for the broad component and with ΔBIC > 10 systematically (see Table 1 and Appendix C). All the fits with the residuals can be seen in Appendix D. On Figure 8, we display the contribution of the broad component to the total Hα luminosity as a function of $\delta^c_{\rm v\text{-}shape}$. A clear trend emerges for compact galaxies. Based on visual only, we fit the relation with a power law of the form $y = A - \left(\frac{x}{x_{\rm median}}\right)^{\gamma}$. By normalizing to the median we help the convergence and avoid degeneracy between the parameters. We infer the two following relations:

$$\frac{L(\mathrm{H}\alpha_{\rm broad})}{L(\mathrm{H}\alpha_{\rm total})} = 1.51^{+0.03}_{-0.03} - \left(\frac{\delta_{\rm v\text{-}shape}}{0.67}\right)^{-1.31^{+0.16}_{-0.14}} \quad (\delta_{\rm compact} > 0.8), \tag{4}$$

We employ an MCMC approach using the `emcee` package to fit the parameters and infer the uncertainties. For extended galaxies, we also detect a correlation that is, however, less strong than for compact galaxies. Due to the lack of S/N of the broad component in extended galaxies that limit the number of bins, we can not conclude wether extended and compact galaxies follow the same relation, but the correlation is still similar for both, indicating a physical connection between the origins of the broad line in extended and compact galaxies. Our results demonstrate a clear three-way correlation: as the V-shape becomes more prominent and the galaxy becomes more compact, the contribution of the broad component increases systematically. No discontinuities or bi-modalities are observed in the behavior of Hα, that reinforce the continuity in the observed properties, identified in Section 4 between the continuum and the compactness.

5.3. Dichotomy of the [NII]

The [N II] line is known to be undetected in LRDs (Matthee et al. 2024; Taylor et al. 2025a; Hviding et al. 2025), hence poorly studied to date, although it could be used as a feature to compare LRDs with the general population. On Figure 9 we display the ratio of the luminosity of the [N II]λ6585 luminosity over the narrow Hα line as a function of $\delta^c_{\rm v\text{-}shape}$. A clear dichotomy apparent between compact and extended galaxies. As expected, we recover the fact that LRDs ($\delta^c_{\rm v\text{-}shape}$>0.6, $\delta_{\rm compact}$>0.8) do not present any [N II] components, but more generally, compact galaxies present a global behavior with an extremely low contribution of [N II]. However, it is not the case for extended galaxies, which present a stronger contribution of [N II] as $\delta^c_{\rm v\text{-}shape}$ increases.

The absence of neutral [N II] in compact galaxies, aside from the LRDs, could indicate either very low metallicity or the presence of nitrogen in a highly ionized state, potentially ionized by a powerful central engine. Given that compact galaxies tend to host a less massive stellar component (Guia et al. 2024), and that less massive galaxies are typically metal-poor (Gallazzi et al. 2005), it is plausible that the metallicity is too low for the [N II] to be detected even in stacked studies. High-ionization lines have been observed in some LRDs, such as N IV$\lambda\lambda$1483, C IV, and [Ne III]λ3869 (Tripodi et al. 2025; Lambrides et al. 2025; Jones et al. 2026), showing that certain complex elements are present in an ionized state. In some LRDs, the metallicity has been inferred and is systematically low, with $Z < 0.1\,Z_\odot$ (e.g., Tripodi et al. 2025; Jones et al. 2026; Maiolino et al. 2025; Ji et al. 2025; Torralba et al. 2026). Moreover, the strong evolution of the broad Hα component with $\delta_{\rm v\text{-}shape}$, contrasted with the lack of evolution in the nitrogen emission for compact galaxies, imply that there is no clear link between the origin of

Table 1. Description of the $\delta_{\text{v-shape}}$ bins for compact sources ($\delta_{\text{compact}} > 0.8$).

Bin range $\delta_{\text{v-shape}}$	$\delta_{\text{v-shape}}$ median	N_{spec}	z median	F444W [mag]	$t_{\text{exp}}{}^{a}$ [10^3s]	Grating^{b} G395M/G395H/G235M	SNR broad	FWHM [km/s]
[0.5, 0.55]	$0.520^{+0.016}_{-0.013}$	147	4.10 ± 1.11	26.28 ± 1.05	153.2	96 / 17 / 34	9.5	1261 ± 56
]0.55, 0.64]	$0.578^{+0.035}_{-0.02}$	58	5.28 ± 1.29	25.88 ± 1.52	59.4	46 / 7 / 5	12.9	2120 ± 84
]0.64, 0.70]	$0.655^{+0.025}_{-0.017}$	20	5.82 ± 1.04	26.08 ± 1.12	20.9	18 / 2 / 0	13.0	2017 ± 81
]0.70, 0.76]	$0.729^{+0.019}_{-0.022}$	17	5.50 ± 0.76	25.46 ± 0.91	16.3	15 / 0 / 2	24.4	2180 ± 40
]0.76, 0.86]	$0.793^{+0.034}_{-0.029}$	22	5.55 ± 1.14	25.74 ± 1.18	21.0	20 / 2 / 0	16.0	2444 ± 86

Notes. $^{(a)}$ Effective exposure time in 10^3s. $^{(b)}$ Number of spectra per grating configuration.

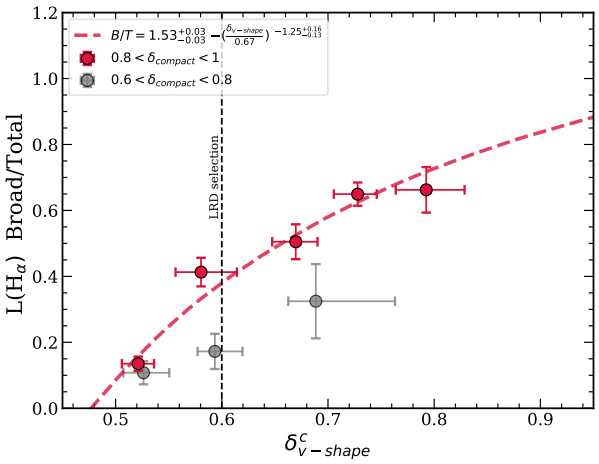

Fig. 8. The contribution of the broad Hα component as a function of the $\delta^{c}_{\text{v-shape}}$ parameter, corrected for the Hα boosting effect. The relation for compact galaxies ($0.6 < \delta_{\text{compact}} < 1$) is shown in red, while that for extended galaxies ($0.6 < \delta_{\text{compact}} < 0.8$) is displayed in gray.

the broad line and the absence of [N II]. However, such a link would be expected if the nitrogen was ionized by the AGN, with the broad line originated from the same AGN, as for instance interpreted in the BPT diagram (Baldwin et al. 1981). This observation also supports the hypothesis of metal-poor compact sources rather than AGN-driven [N II] emission. This aligns with the findings of Kocevski et al. (2023) and Harikane et al. (2023), which highlight the limitations of the BPT diagram at high redshift for diagnosing AGNs in metal-poor environments. The behavior observed is also consistent with the results for extended galaxies, which systematically exhibit a more significant [N II] contribution. The stellar component in extended galaxies naturally increases with metallicity, allowing the detection of [N II]. If the broad-line in extended galaxies is interpreted as a proxy for the central BH mass, it suggests that the more massive the central BH, the more prominent the nitrogen emission. This can be interpreted similarly to regular AGN or through the BPT diagram: the more powerful the central AGN, the more likely we are to observe the [N II] line.

To further investigate the metallicity, we computed the O32 and Ne3O2 parameters. Following the methodology presented in Section 5.1, we stacked the PRISM spectra as a function of $\delta_{\text{v-shape}}$, restricting the selection to sources with $4 < z < 7$ to minimize to probe to different epoch, as metallicity is known to evolve with redshift (e.g., Maiolino et al. 2008; Sanders et al. 2021). Another parameter widely used is the R23 parameter, define as $R_{23} = ([O_{III}]\lambda4963, 5007 + [O_{II}]\lambda3727)/H\beta$. Since R23 is normalized by Hβ, which likely presents a non negligible contribution from the central engine in the LRD context, we excluded it from our work.

O32 is defined as $O_{32} = [O_{III}]\lambda5007/[O_{II}]\lambda\lambda3727, 29$ and Ne3O2 as Ne302=$[Ne_{III}]\lambda3870/[O_{II}]\lambda3728$. Once computed, we translate both parameters into metallicity ($12 + \log(O/H)$), using the calibration inferred for high-redshift galaxies ($2 < z < 9$) by Sanders et al. (2021). In Figure 10, we display the mean metalicity inferred from the O32 and Ne3O2. We recover the dichotomy we observed on the [N II]: compact galaxies tend to be metal poor ($Z < 0.1Z_{\odot}$) compared to extended galaxies ($Z > 0.1Z_{\odot}$). This implies that LRDs are metal-poor primarily because of their compactness rather than their classification as LRDs. Within the broader population of compact objects, we however tend to identify a further evolution toward lower metallicities as the V-shape intensity increases, potentially probing lower-mass host galaxies compared to other compact systems.

The emission lines used to derive metallicities in this work can be affected by high electron densities (n_e), which may trigger collisional de-excitation in dense environments. However, several features suggest that the [O III] and UV emission originate from the host galaxy rather than the dense central engine. These include the observed correlation between [O III] luminosity and M_{UV} (de Graaff et al. 2025b), the lack of UV variability (Furtak et al. 2025), and the presence of extended UV emission (Rinaldi et al. 2025b; Chen et al. 2025; Baggen et al. 2026). Consequently, the low metallicities inferred for LRDs and compact galaxies favor a low-mass host scenario (e.g., de Graaff et al. 2025b; Sun et al. 2026b). This is consistent with a young stellar component, which has been previously proposed to explain the rest-frame UV emission in LRDs (e.g., Taylor et al. 2025b; Delvecchio et al. 2025; Torralba et al. 2026; Barro et al. 2026).

6. Balmer Decrement

The Balmer decrement observed in LRDs is surprisingly high, reaching values comparable to those found in heavily obscured dusty galaxies: Hα/H$\beta \approx 10$; e.g., de Graaff et al. 2025b and even ≈ 16 in the BH* interpretation (Sun et al. 2026b). Following the procedure described in Section 5.3, we stack the PRISM data and perform line fitting using BADASS, focusing on the 0.45–0.70 μm rest-frame range to capture both Hβ and Hα. We compute the observed Balmer decrement as a function of $\delta^{c}_{\text{v-shape}}$ and δ_{compact}, for sources between $4 < z < 7$, as shown on Figure 11. Our results confirm that in the LRD regime, the Balmer decrement is significantly elevated (≈ 10). More generally, we find that the Balmer decrement correlates strongly with $\delta^{c}_{\text{v-shape}}$, regardless of the galaxy's compactness. This suggest that both

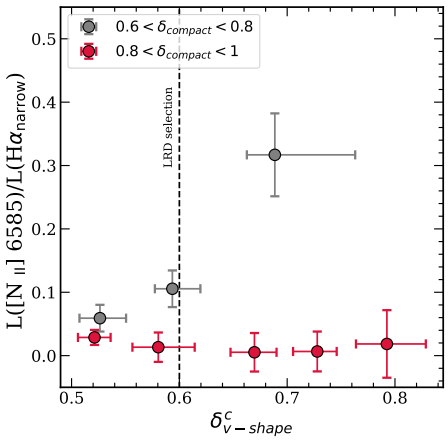

Fig. 9. Contribution of the [NII 6585] to the Hα narrow line, as a function of $\delta^c_{\text{v-shape}}$, for compact (in red) and extended galaxies (in gray).

the V-shape intensity and the Balmer decrement share common physical origins.

The dotted and dash-dotted lines represent the expected Balmer decrement derived from dust attenuation, assuming two different laws: Calzetti et al. (2000a) and Gordon et al. (2003). These predictions were calculated by measuring the median optical slope (β_{opt}) within each $\delta^c_{\text{v-shape}}$ bin, which was then translated into a visual attenuation (A_V) and converted into an expected Hα/Hβ ratio. Since we derive the attenuation from the rest-frame optical slope, the age of the stellar population can influence the underlying intrinsic slope, $\beta_{\text{opt,int}}$ (i.e., the slope in the absence of dust). To constrain $\beta_{\text{opt,int}}$, we modeled the SEDs of star-forming galaxies using CIGALE (Boquien et al. 2019), with stellar ages ranging from 0.1 to 1.5 Gyr (where $\approx$ 1.5 Gyr corresponds to the age of the Universe at $z \approx 4$). We found that the intrinsic optical slopes vary between -2.3 and -1.8. For both these value we computed the predicted Balmer decrement and show it on Figure 11.

As visible, the observed increase in Hα/Hβ with $\delta^c_{\text{v-shape}}$ is consistent with a dust-dominated interpretation across the entire sample, even within the LRD regime.

More precisely, the majority of the data appear consistent with a Calzetti et al. (2000a) attenuation law, except for the highest V-shape intensity and compactness sources, which exhibit a Balmer decrement lower than the values predicted by this attenuation law. This deviation suggests a shift in the underlying physical processes, such as a change in the dust grain size distribution or a dependence on metallicity. Indeed, these sources diverge toward the Small Magellanic Cloud (SMC) attenuation law (Gordon et al. 2003), which is typically better suited for the low-metallicity environments, as Figure 10 showed.

Adopting the SMC attenuation law, we derive A_V from Hα/Hβ in the LRD regime (last 3 red points on Figure 11). Following the methodology of Casey et al. (2024) and using the median R_e in each bin (provided by Genin et al. 2025 on the DJA), we convert A_V into an estimated dust mass. This provides a robust constraint on the dust content of LRDs, which, based on the Balmer decrement, is estimated to be $M_{\text{dust, LRDs}} \approx 4{-}7{\times}10^4\ M_\odot$. This is consistent with the results of Casey et al. (2024), who used an A_V derived from SED fitting. This implies that even a very small amount of dust, if present in LRDs, can reproduce the observed Balmer decrements and contribute to the red colors in LRDs. Alternatively, de Graaff et al. (2025b) suggested that the Balmer decrement might reflect the physical conditions of a dense gas medium, where scattering and collisional deexcitation dominate the formation of high Hα/Hβ ratios. The dust mass estimated here can therefore be interpreted as an upper limit.

Since we observe a similar correlation between non-LRD and LRD sources, as well as a continuous transition as sources approach high LRD states, and given that the Balmer decrement is driven by dust in the non-LRD regime, this suggests that dust could also be responsible for the observed Balmer decrement in LRDs. As showed by Casey et al. (2024), current ALMA observations lack the sensitivity to probe the predicted L_{IR} in LRDs, and imply that the presence of dust can not be excluded.

Moreover, within the BH* framework, the predicted Balmer decrement is highly sensitive to the gas column density, $N_{\text{HI,2s}}$ (see Figure 5 in Chang et al. 2026). If the entire LRD population were effectively composed of BH* with $N_{\text{HI,2s}} > 10^{14}\text{cm}^{-2}$, a clear discontinuity with the galaxy field would be expected, which is not observed.

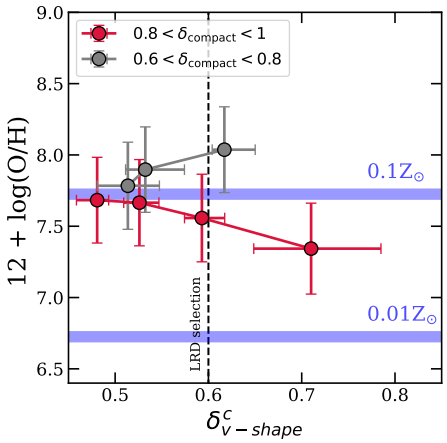

Fig. 10. Metallicity inferred with the O32 and Ne3O2 parameters between 4<z<7, as a function of $\delta_{\text{v-shape}}$. Red circles denotes compact galaxies, whereas gray circles represent extended galaxies.

7. Discussion

In this section, we synthesize our findings and discuss their interpretation within the context of LRDs. We first establish that the continuum shape of all galaxies is strongly correlated with morphology, as galaxies exhibiting a pronounced V-shape tend to be more compact (see Figure 5-left). Moreover, we observe a smooth progression toward the LRD state, with no evidence of a sharp discontinuity around standard LRD selection criteria.

We further demonstrate that broad-line intensity is also strongly correlated with the shape of the continuum as probed by the *V-shapeness* measured by our parameter $\delta_{\text{v-shape}}$, indicating a clear connection between these three properties (see Figure 8). While this trend is more pronounced in compact sources, it persists among extended sources as well. Although compact, V-shaped sources are more likely to exhibit non-stellar Balmer breaks, with values close to unity (see Figure 6). Additionally, compact sources generally lack a significant [NII] component, whereas [NII] emission tends to be more prominent in extended galaxies (see Figure 9). We interpret this as a direct consequence of lower metallicity in compact galaxies, an hypothesis further supported by metallicity estimates inferred from the O32 and Ne3O2 parameters. The Balmer decrement scales strongly with the inten-

sity of the V-shape, as more pronounced V-shaped sources exhibit a higher Hα/Hβ ratio. Furthermore, extended galaxies show a higher decrement at a given V-shape intensity.

In particular, all these trends are continuous, with no observed discontinuities near the boundaries of LRD selections. This suggests a gradual progression toward the LRD state rather than a discrete "on-off" transition that would define LRDs as a strictly distinct population, undergoing different physical processes.

The first key property we infer is that the origin of the broad-line emission is intrinsically linked to the optical continuum, as evidenced by their strong correlation across all observed morphologies. In the framework of the BH* interpretation (Naidu et al. 2025; de Graaff et al. 2025c,b; Begelman & Dexter 2026; Barro et al. 2026; Sun et al. 2026b), line broadening does not arise from gas kinematics, as in the classical AGN paradigm involving the BLR, but rather from interactions between photons and dense layers of gas surrounding the central black hole. The analysis of Chang et al. (2026) accounted for several physical processes, including resonance scattering of Balmer lines, Raman scattering, and Thomson scattering. However, several of our findings appear inconsistent with the possibility that the BH* model, as currently proposed, can explain the entire LRD population. The absence of discontinuities, near or above standard LRD selection thresholds (see Figure 8), suggests that the physical mechanism responsible for broad-lines in non-LRD galaxies ($\delta_{\text{v-shape}} < 0.6$) remains present in the LRD regime ($\delta_{\text{v-shape}} > 0.6$). This reveals a clear evolutionary or physical link between non-V-shaped broad Hα emitters, typically classified as regular AGNs, and LRDs. Since the broad-lines in the AGN paradigm arise from virialized motion within the BLR, the black hole mass is directly linked to the width of the observed lines through the relation $M_{\text{BH}} \propto R\Delta V^2/G$, (e.g., Greene & Ho 2005; Reines & Volonteri 2015). While the BH* interpretation invokes purely interactions with dense gas, a fundamental dissonance emerges between these two models for what appears to be a single, continuous population. Again, this applies to the bulk of the LRD population and does not prevent some LRDs to present unique features, or being pure BH*.

As discussed in Section 4.1, non-stellar Balmer breaks are exclusively observed in compact, V-shaped galaxies but does not account for the majority. In de Graaff et al. (2025b), the strength of these non-stellar Balmer breaks is modeled using a modified blackbody with $T_{\text{BB}} \approx 5000$ K. Combined with the absorption features detected in several LRDs (e.g., Kocevski et al. 2025; Matthee et al. 2024; Barro et al. 2026), it suggests the presence of a high-density gas reservoir along the line of sight (Inayoshi & Maiolino 2025; D'Eugenio et al. 2025; de Graaff et al. 2025c; Naidu et al. 2025) in several LRDs. Given the continuous transition toward the LRD state identified in our work, a corresponding continuity in physical processes is expected between AGNs and LRDs.

This continuity suggests that the majority of LRDs likely possess BLR responsible for line broadening, analogous to standard AGNs. Similarly, the observed continuity in the Balmer decrement implies that dust should also be considered to explain the red colors in LRDs, as current observations cannot definitively exclude this hypothesis. This interpretation further implies that dense gas is unlikely to be the sole physical process responsible for either line broadening or the reddening observed in LRDs. While the dense gas reservoir invoked in the BH* framework may apply to specific LRD sources, these configurations are likely transient. Over time, such systems may either self-disrupt or evolve kinematically through interactions

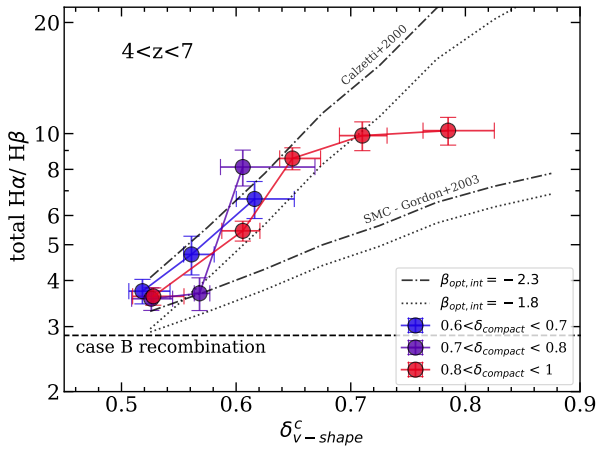

Fig. 11. Observed Balmer decrement as a function of $\delta^c_{\text{v-shape}}$, for different bins of compactness δ_{compact}. The dotted line represent the Case B recombination and the other lines (dotted & dash-dotted) the Balmer decrement expected from dust attenuation.

with the central black hole and its environment. This process would render extreme configurations short-lived, consistent with our findings that more extreme sources exhibit shorter lifetimes (see Section 4). Such evolution could ultimately lead to the fragmentation of the gas into dense clouds, forming the BLR, while simultaneously reducing the overall gas density in the surrounding environment. This reduction in density would, in turn, result in Balmer break strengths consistent with those observed in typical AGNs (Inayoshi & Maiolino 2025). A recent model proposed by Madau & Maiolino (2026) reinforces this perspective, interpreting the LRD population as Type 1 AGNs observed within a specific range of geometric configurations and inclination angles. Under this framework, LRDs do not constitute a distinct class of objects but rather represent the extreme tail of the Type 1 AGN distribution, featuring a BLR composed of dense gas clumps. This is further supported by recent discoveries of LRDs transitioning into typical AGNs, as well as X-ray detections in several sources (Kocevski et al. 2025; Fu et al. 2025; Hviding et al. 2026). These detections suggest that the gas has become sufficiently diffuse along the line of sight to allow X-ray photons to escape, thereby probing a lower-density environment than previously observed.

8. Conclusion

In this work, we investigate whether LRDs represent a distinct class of astronomical objects or if they are instead in continuity with the broader galaxy population. To do so, we combine photometric, spectroscopic, and morphological data over ≈ 750 arcmin^2 and introduce a continuous metric to evaluate the defining features of LRDs. This approach allows us to avoid arbitrary selection effects, which could otherwise introduce a biased view of the population.

A clear connection emerges between their three primary features: morphology, V-shaped SED prominence, and broad-line strength. Specifically, as the V-shaped SED becomes more pronounced, the morphology becomes increasingly compact, which correlates with a rising contribution from the broad emission line component. Crucially, we find no discontinuities between the conventionally selected LRD population and the general galaxy population. Instead, we observe a smooth transi-

tion between the intensity of the V-shape and both the fraction of compact galaxies (see Figure 5, left) and the broad-line contribution to the Hα complex (see Figure 8). This suggests that LRDs are not a separate class of objects, but rather the extreme end of a continuum defined by increasing compactness, V-shape intensity, and line broadening.

Furthermore, extreme Balmer breaks (exceeding 3) are predominantly found in the most extreme LRD states. However, these account for only $\approx$ 3% of the sample, suggesting that such rare sources represent a short-lived evolutionary phase and contribute to the overall heterogeneity of the population.

LRDs present a deficit in [N II] but we find that this deficit is not restricted to them (see Figure 9). Instead, it appears to be a global property of compact, metal-poor sources, indicating a low mass host.

The observed continuity in the presence and relative intensities of broad Hα lines suggests that the physical mechanisms responsible for line broadening in LRDs are consistent with the presence of a BLR, as in the standard AGN paradigm.

Another sign of similarity, the continuity between LRD and non-LRD galaxies in the intensity of their Balmer decrement suggests that the red color of LRDs is dominantly due to dust attenuation. Since current observations cannot definitively exclude the presence of dust, its potential role should not be dismissed. Assuming the Balmer decrement is solely produced by dust, we infer an upper limit for the dust mass in LRDs of $M_{\rm dust,\,LRDs} \approx 4 - 7 \times 10^4\ M_\odot$.

Acknowledgements. This work is based on observations made with the NASA/ESA/CSA James Webb Space Telescope (JWST). The data were obtained from the Mikulski Archive for Space Telescopes at the Space Telescope Science Institute, which is operated by the Association of Universities for Research in Astronomy, Inc., under NASA contract NAS 5-03127 for JWST. These observations are associated with JWST programs ERS-1345 (CEERS), GO-1837 (PRIMER), GO-2561 (UNCOVER), GO-4233 (RUBIES), as well as GTO programs 1180, 1181, 1210, 1215, 1286, 1287 (JADES). We also acknowledge the DAWN JWST Archive (DJA), for providing the reduced data products and photometric catalogs used in this analysis. This project has received funding from the European Union's Horizon 2020 research and innovation programme under the Marie Skłodowska-Curie grant agreement No 101148925. We would acknowledge the following open source software used in the analysis: `Astropy` (Astropy Collaboration et al. 2022) , `photutils` (Bradley et al. 2024), `Numpy` (Harris et al. 2020).

References

Akins, H. B., Casey, C. M., Lambrides, E., et al. 2025, ApJ, 991, 37
Arnouts, S., Cristiani, S., Moscardini, L., et al. 1999, MNRAS, 310, 540
Astropy Collaboration, Price-Whelan, A. M., Lim, P. L., et al. 2022, ApJ, 935, 167
Baggen, J. F. W., Scoggins, M. T., van Dokkum, P., et al. 2026, arXiv e-prints, arXiv:2602.02702
Baldwin, J. A., Phillips, M. M., & Terlevich, R. 1981, PASP, 93, 5
Barro, G., Perez-Gonzalez, P. G., Kocevski, D. D., et al. 2024, arXiv e-prints, arXiv:2412.01887
Barro, G., Pérez-González, P. G., Kocevski, D. D., et al. 2026, ApJ, 997, 48
Begelman, M. C. & Dexter, J. 2026, ApJ, 996, 48
Begelman, M. C., Rossi, E. M., & Armitage, P. J. 2008, MNRAS, 387, 1649
Bezanson, R., Labbe, I., Whitaker, K. E., et al. 2024, ApJ, 974, 92
Billand, J.-B., Elbaz, D., Gentile, F., et al. 2026, A&A, 706, A29
Boquien, M., Burgarella, D., Roehlly, Y., et al. 2019, A&A, 622, A103
Bradley, L., Sipőcz, B., Robitaille, T., et al. 2024, astropy/photutils: 2.0.2
Brammer, G. 2023, msaexp: NIRSpec analysis tools, https://zenodo.org/records/8319596
Brammer, G. B., van Dokkum, P. G., & Coppi, P. 2008, ApJ, 686, 1503
Brazzini, M., D'Eugenio, F., Maiolino, R., et al. 2025, MNRAS, 544, L167
Brooks, M., Trump, J. R., Simons, R. C., et al. 2025, arXiv e-prints, arXiv:2511.19609
Calzetti, D., Armus, L., Bohlin, R. C., et al. 2000a, ApJ, 533, 682
Calzetti, D., Armus, L., Bohlin, R. C., et al. 2000b, ApJ, 533, 682
Casey, C. M., Akins, H. B., Kokorev, V., et al. 2024, ApJ, 975, L4
Chang, S.-J., Gronke, M., Matthee, J., & Mason, C. 2026, MNRAS, 545, staf2131
Chen, C.-H., Ho, L. C., Li, R., & Zhuang, M.-Y. 2025, ApJ, 983, 60
Cox, I. G., Kartaltepe, J. S., Bagley, M. B., et al. 2025, arXiv e-prints, arXiv:2510.08743
Curtis-Lake, E., Cameron, A. J., Bunker, A. J., et al. 2025, arXiv e-prints, arXiv:2510.01033
Davis, M., Guhathakurta, P., Konidaris, N. P., et al. 2007, ApJ, 660, L1
de Graaff, A., Brammer, G., Weibel, A., et al. 2025a, A&A, 697, A189
de Graaff, A., Hviding, R. E., Naidu, R. P., et al. 2025b, arXiv e-prints, arXiv:2511.21820
de Graaff, A., Rix, H.-W., Naidu, R. P., et al. 2025c, A&A, 701, A168
Delvecchio, I., Daddi, E., Magnelli, B., et al. 2025, A&A, 704, A313
D'Eugenio, F., Cameron, A. J., Scholtz, J., et al. 2025, ApJS, 277, 4
Dunlop, J. S., Abraham, R. G., Ashby, M. L. N., et al. 2021, PRIMER: Public Release IMaging for Extragalactic Research, JWST Proposal. Cycle 1, ID. #1837
Eisenstein, D. J., Willott, C., Alberts, S., et al. 2026, ApJS, 283, 6
Finkelstein, S. L., Bagley, M. B., Arrabal Haro, P., et al. 2025, ApJ, 983, L4
Finkelstein, S. L., Bagley, M. B., Ferguson, H. C., et al. 2023, ApJ, 946, L13
Finkelstein, S. L., Dickinson, M., Ferguson, H. C., et al. 2017, The Cosmic Evolution Early Release Science (CEERS) Survey, JWST Proposal ID 1345. Cycle 0 Early Release Science
Ford, H. C., Bartko, F., Bely, P. Y., et al. 1998, in Society of Photo-Optical Instrumentation Engineers (SPIE) Conference Series, Vol. 3356, Space Telescopes and Instruments V, ed. P. Y. Bely & J. B. Breckinridge, 234–248
Fu, S., Zhang, Z., Jiang, D., et al. 2025, arXiv e-prints, arXiv:2512.02096
Furtak, L. J., Secunda, A. R., Greene, J. E., et al. 2025, A&A, 698, A227
Furtak, L. J., Zitrin, A., Plat, A., et al. 2023, ApJ, 952, 142
Gallazzi, A., Charlot, S., Brinchmann, J., White, S. D. M., & Tremonti, C. A. 2005, MNRAS, 362, 41
Genin, A., Shuntov, M., Brammer, G., et al. 2025, A&A, 699, A343
Gordon, K. D., Clayton, G. C., Misselt, K. A., Landolt, A. U., & Wolff, M. J. 2003, ApJ, 594, 279
Greene, J. E. & Ho, L. C. 2005, ApJ, 630, 122
Greene, J. E., Labbe, I., Goulding, A. D., et al. 2024, The Astrophysical Journal, 964, 39, publisher: The American Astronomical Society
Guia, C. A., Pacucci, F., & Kocevski, D. D. 2024, Research Notes of the American Astronomical Society, 8, 207
Hainline, K. N., Johnson, B. D., Robertson, B., et al. 2024, ApJ, 964, 71
Harikane, Y., Zhang, Y., Nakajima, K., et al. 2023, A JWST/NIRSpec First Census of Broad-line AGNs at z = 4-7: Detection of 10 Faint AGNs with M $_{BH}$ 10^6-10^8 M $_\odot$ and Their Host Galaxy Properties
Harris, C. R., Millman, K. J., van der Walt, S. J., et al. 2020, Nature, 585, 357
Heintz, K. E., Brammer, G. B., Watson, D., et al. 2025, A&A, 693, A60
Hviding, R. E., de Graaff, A., Liu, H., et al. 2026, ApJ, 1000, L18
Hviding, R. E., de Graaff, A., Miller, T. B., et al. 2025, A&A, 702, A57
Ilbert, O., Arnouts, S., McCracken, H. J., et al. 2006, A&A, 457, 841
Inayoshi, K. & Maiolino, R. 2025, ApJ, 980, L27
Ji, X., Maiolino, R., Übler, H., et al. 2025, MNRAS, 544, 3900
Jones, G. C., Übler, H., Maiolino, R., et al. 2026, MNRAS, 546, stag115
Juodžbalis, I., Maiolino, R., Baker, W. M., et al. 2026, MNRAS, 546, stag086
Juodžbalis, I., Marconcini, C., D'Eugenio, F., et al. 2025, arXiv e-prints, arXiv:2508.21748
Kido, D., Ioka, K., Hotokezaka, K., Inayoshi, K., & Irwin, C. M. 2025, MNRAS, 544, 3407
Kocevski, D. D., Finkelstein, S. L., Barro, G., et al. 2025, ApJ, 986, 126
Kocevski, D. D., Onoue, M., Inayoshi, K., et al. 2023, ApJ, 954, L4
Kokorev, V., Caputi, K. I., Greene, J. E., et al. 2024, ApJ, 968, 38
Labbe, I., Greene, J. E., Bezanson, R., et al. 2025, ApJ, 978, 92
Labbé, I., Van Dokkum, P., Nelson, E., et al. 2023, Nature, 616, 266
Lambrides, E., Larson, R., Hutchison, T., et al. 2025, arXiv e-prints, arXiv:2509.09607
Leung, G. C. K., Finkelstein, S. L., Pérez-González, P. G., et al. 2025, ApJ, 992, 26
Ma, Y., Greene, J. E., Setton, D. J., et al. 2026, ApJ, 1000, 59
Ma, Y., Greene, J. E., Setton, D. J., et al. 2025, ApJ, 981, 191
Madau, P. & Maiolino, R. 2026, arXiv e-prints, arXiv:2602.22386
Maiolino, R., Nagao, T., Grazian, A., et al. 2008, A&A, 488, 463
Maiolino, R., Uebler, H., D'Eugenio, F., et al. 2025, arXiv e-prints, arXiv:2505.22567
Maseda, M. V., de Graaff, A., Franx, M., et al. 2024, A&A, 689, A73
Matthee, J., Naidu, R. P., Brammer, G., et al. 2024, ApJ, 963, 129
Naidu, R. P., Matthee, J., Katz, H., et al. 2025, arXiv e-prints, arXiv:2503.16596

Oke, J. B. 1974, ApJS, 27, 21
Osterbrock, D. E. & Ferland, G. J. 2006, Astrophysics of gaseous nebulae and active galactic nuclei
Pacucci, F., Ferrara, A., & Kocevski, D. D. 2026, arXiv e-prints, arXiv:2601.14368
Pacucci, F., Nguyen, B., Carniani, S., Maiolino, R., & Fan, X. 2023, ApJ, 957, L3
Pérez-González, P. G., Barro, G., Rieke, G. H., et al. 2024, ApJ, 968, 4
Planck Collaboration, Aghanim, N., Akrami, Y., et al. 2020, A&A, 641, A6
Price, S. H., Bezanson, R., Labbe, I., et al. 2025, ApJ, 982, 51
Reines, A. E. & Volonteri, M. 2015, ApJ, 813, 82
Rieke, M. J., Robertson, B., Tacchella, S., et al. 2023, ApJS, 269, 16
Rinaldi, P., Bonaventura, N., Rieke, G. H., et al. 2025a, ApJ, 992, 71
Rinaldi, P., Rieke, G. H., Wu, Z., et al. 2025b, arXiv e-prints, arXiv:2507.17738
Rusakov, V., Watson, D., Nikopoulos, G. P., et al. 2026, Nature, 649, 574
Sanders, R. L., Shapley, A. E., Jones, T., et al. 2021, ApJ, 914, 19
Santarelli, A. D., Farag, E., Bellinger, E. P., et al. 2026, ApJ, 998, L4
Scholtz, J., Carniani, S., Parlanti, E., et al. 2025, arXiv e-prints, arXiv:2510.01034
Setton, D. J., Greene, J. E., Spilker, J. S., et al. 2025, ApJ, 991, L10
Sexton, R. O., Matzko, W., Darden, N., Canalizo, G., & Gorjian, V. 2021, MNRAS, 500, 2871
Shen, Y., Zhuang, M.-Y., Li, J., et al. 2024, arXiv e-prints, arXiv:2408.12713
Shuntov, M., Akins, H. B., Paquereau, L., et al. 2025, A&A, 704, A339
Sun, H., Wang, T., Xu, K., et al. 2026a, arXiv e-prints, arXiv:2603.05289
Sun, W. Q., Naidu, R. P., Matthee, J., et al. 2026b, arXiv e-prints, arXiv:2601.20929
Taylor, A. J., Finkelstein, S. L., Kocevski, D. D., et al. 2025a, ApJ, 986, 165
Taylor, A. J., Kokorev, V., Kocevski, D. D., et al. 2025b, ApJ, 989, L7
Torralba, A., Matthee, J., Pezzulli, G., et al. 2026, A&A, 707, A75
Tripodi, R., Martis, N., Markov, V., et al. 2025, Nature Communications, 16, 9830
Williams, C. C., Alberts, S., Ji, Z., et al. 2024, The Astrophysical Journal, 968, 34, publisher: The American Astronomical Society
Xiao, M., Oesch, P. A., Bing, L., et al. 2025, A&A, 700, A231

Appendix A: Compactness with aperture photometry

In this section, we compare the aperture photometry ratios to ensure that the $\delta_{\rm compact}$ parameter, defined as the ratio $f_{444}(0.36'')/f_{444}(0.5'')$, is capable of effectively probing compact objects, similar to the C_{444} parameter used in Akins et al. (2025), which is defined as $f_{444}(0.2'')/f_{444}(0.5'')$. In Figure A.1, we focus on PRIMER-COSMOS, for which the C_{444} values are provided by the COSMOS-Web catalog (Shuntov et al. 2025). Both parameters are strongly correlated with small intrinsic scatter implying that, like C_{444}, $\delta_{\rm compact}$ is an efficient proxy for identifying compact sources.

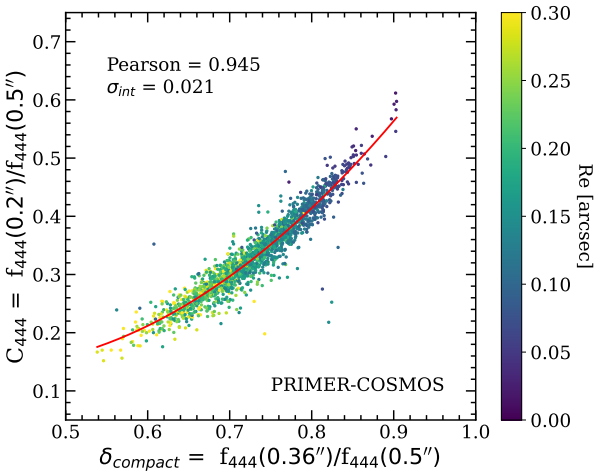

Fig. A.1. C_{444} as a function of $\delta_{\rm compact}$. The red curve corresponds to the best polynomial fit, while the colormap indicates the effective radius (R_e) from the 2D Sersic fit provided by the DJA (Genin et al. 2025). Both the Pearson correlation coefficient and the intrinsic scatter of the best fit are also shown.

Appendix B: Sigmoid function

To investigate the fraction of compact galaxies as a function of the V-shape intensity, $\delta_{\rm v\text{-}shape}$, and redshift, we observe that the relationship at each redshift can be effectively described by a sigmoid function. We therefore fit the data using the following formula:

$$y = \frac{L}{1 + e^{-k(x-x_0)}} + b, \tag{B.1}$$

where x represents $\delta_{\rm v\text{-}shape}$, x_0 is the median value of the sample ($\delta_{\rm v\text{-}shape,\ median}$), and y corresponds to $\delta_{\rm compact}$. In Figure B.1, the dashed lines represent the best-fit sigmoid curves for each redshift bin, while the shaded regions indicate the uncertainties in the fit, derived through a Monte Carlo approach.

Appendix C: BIC comparison

To assess the presence of broad lines, we utilized the Bayesian Information Criterion (BIC), defined as:

$$\mathrm{BIC} = \chi^2 + k \times \log(n), \tag{C.1}$$

where k is the number of free parameters in the model, and n is the number of data points. We computed the BIC for models

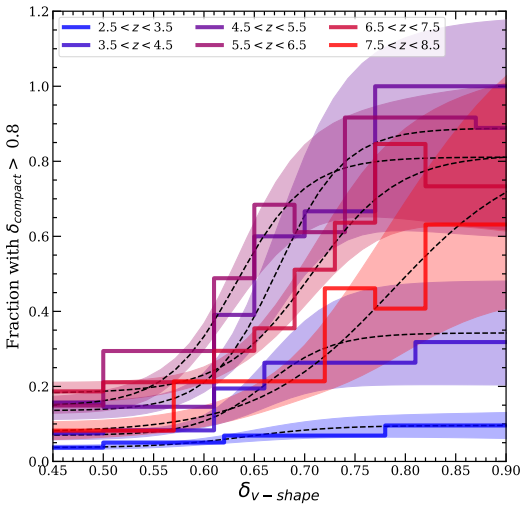

Fig. B.1. Fraction of galaxies with $\delta_{\rm compact} > 0.8$ as a function of $\delta_{\rm v\text{-}shape}$, shown for redshift bins ranging from $z = 3 \pm 0.5$ to $z = 8 \pm 0.5$. The solid lines represent the observed data, while the dashed lines indicate the best-fit sigmoid models, with the associated uncertainties depicted as shaded regions.

both with and without a broad component. Figure C.1 illustrates the difference between the two BIC values, ΔBIC, for our compact sample in red ($\delta_{\rm compact} > 0.8$) and our extended sample in gray ($\delta_{\rm compact} < 0.8$). As detailed in Section 5, we consider a broad line to be reliably detected and necessary when ΔBIC > 5 and the S/N of the broad component exceeds 5.

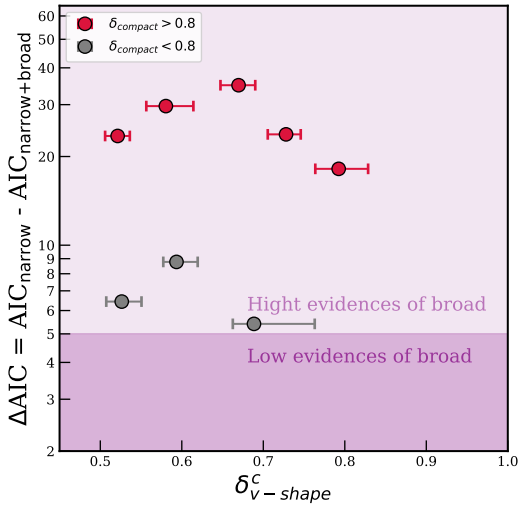

Fig. C.1. Comparison of BIC for models with and without a broad component. Compact sources are represented by red circles, while extended sources are shown as gray circles.

Appendix D: Hα line fit

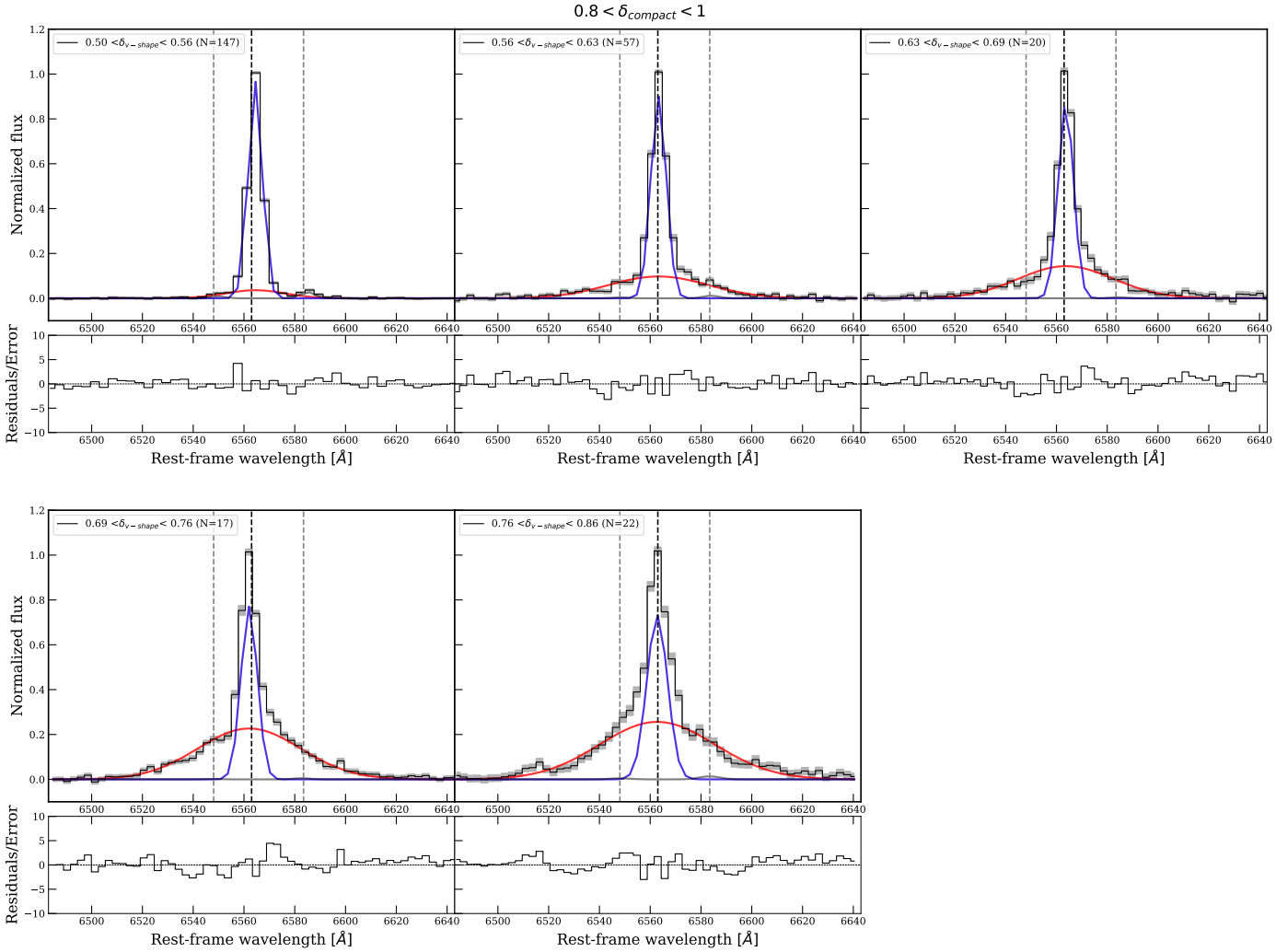

Fig. D.1. Results of the Hα complex fit for the compact galaxy group ($0.8 < \delta_{\rm compact} < 1$). The broad H$\alpha$ component is shown in red, while the narrow component is in blue. The [NII] doublet is also displayed in solid light gray, for each bin of $\delta^{c}_{\rm v\text{-}shape}$.

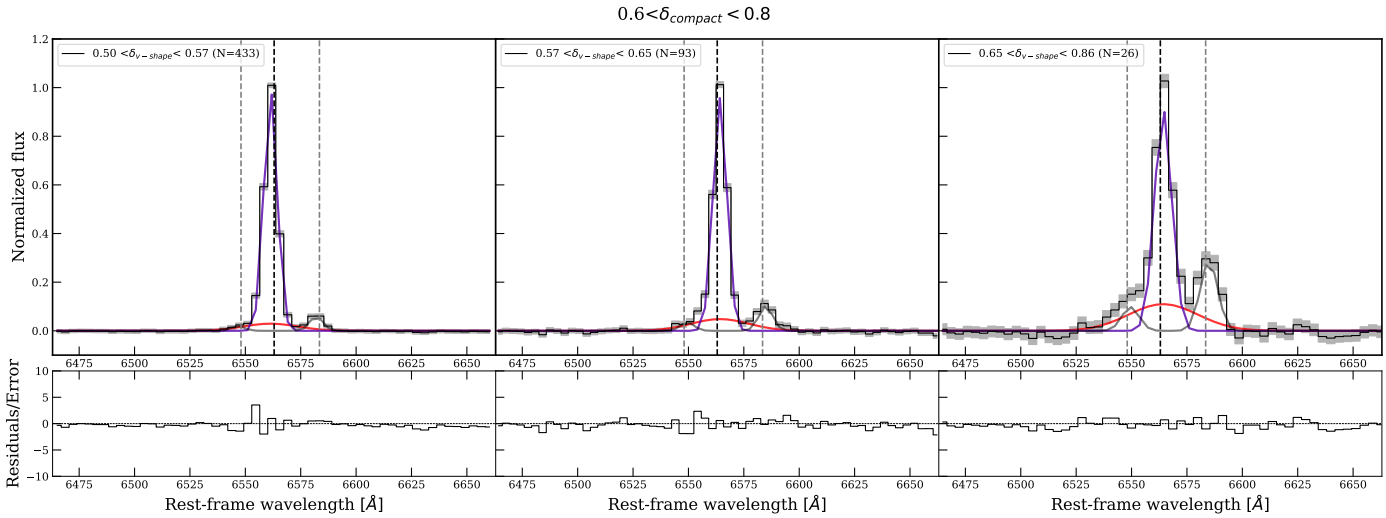

Fig. D.2. Same as Figure D.1 but for extended sources ($0.6 < \delta_{\rm compact} < 0.8$).